AIAA JOURNAL
Vol. 31, No. 9, September 1993

Euler Calculations of Unsteady Interaction of Advancing Rotor with a Line Vortex

G. R. Srinivasan* and W. J. McCroskey†
NASA Ames Research Center, Moffett Field, California 94035

The unsteady, three-dimensional flowfield of a helicopter rotor blade in forward flight encountering a concentrated line vortex is calculated using an implicit, finite difference numerical procedure for the solution of Euler equations. A prescribed vortex method is adopted to preserve the structure of the interacting vortex. The test cases considered for computation correspond to the two-bladed model rotor experimental conditions of Caradonna et al. and consist of parallel and oblique interactions. Comparison of numerical results with the test data show good agreement for the surface pressures for both parallel and oblique interactions at subsonic and transonic flow conditions. The results indicate that the subsonic parallel blade-vortex interaction is nearly two-dimensional-like and the unsteady time-lag effects appear to be negligible. However, both the three-dimensional and unsteady time-lag effects are found to be important under supercritical flow conditions and these effects are accentuated in the presence of transonic shocks. In contrast, the oblique blade-vortex interaction is unsteady and three dimensional at both the subsonic and transonic flow conditions.

Nomenclature

a	= speed of sound
a_o	= vortex core radius, see Eq. (8)
C	= characteristic length scale, chord of the rotor blade
C_k	= constant, see Eq. (8)
C_p	= pressure coefficient based on local dynamic pressure
C_w	= chord of the vortex generating wing
e	= total energy per unit volume
$\hat{F}, \hat{G}, \hat{H}$	= flux vectors
J	= Jacobian of the coordinate transformation
M_∞	= freestream Mach number, forward speed of the rotor
M_{tip}	= tip Mach number of the rotor blade
p	= static pressure
$\hat{Q}$	= vector of conserved flow variables
R	= rotor radius
r	= radial distance from the vortex center
r_B	= rotor reference station normalized by R
$\Re(t)$	= rotational matrix, see Eq. (4)
U, V, W	= contravariant velocity components
u_∞	= forward flight speed
u, v, w	= velocity components in physical space
v_θ	= tangential velocity of the vortex
x, y, z, t	= inertial coordinates
x_o, z_o	= vortex offset position relative to the rotor axis
$\tilde{x}_v, \tilde{z}_v$	= distance from blade leading edge to the line vortex
$\tilde{x}, \tilde{y}, \tilde{z}, \tilde{t}$	= blade-fixed coordinates
γ	= ratio of specific heats
Γ	= vortex strength
$\hat{\Gamma}$	= dimensionless strength of the vortex, $\Gamma/(a_\infty C)$
μ	= advance ratio, $u_\infty/\Omega R$
ξ, η, ζ, τ	= generalized curvilinear coordinates
ρ	= density
Ψ	= azimuthal angle
Ω	= angular velocity of the rotor

Subscripts

∞	= freestream
o	= interacting vortex flowfield

Introduction

THE accurate simulation of the flowfield of a helicopter rotor is still one of the most complex and challenging problems of applied aerodynamics. This is true in spite of the availability of the present-day supercomputers of Cray-2 class and improved numerical algorithms. The major reason for this is that the flowfield of a rotor in forward flight is very complex. It is highly three dimensional, unsteady, and viscous, with pockets of transonic flow near the blade tips on the advancing blades and regions of dynamic stall on the retreating blades. In addition, the blades also shed complex vortical wakes. The concentrated tip vortices shed by these blades generally have a close encounter with the following blades. Such a close encounter of the force-free concentrated vortices with the rotor blades is often the cause of unsteady load fluctuations and impulsive noise. These and other complex problems associated with such a flowfield are delineated in a schematic of a helicopter in forward flight in Fig. 1.

The spiralling vortex sheet emanating from each of the blades of the rotor has a profound influence on the performance of the helicopter. It not only alters the effective pitch angle of the blades and thus the airloads, but also produces highly nonlinear interactions of the vortex with the rotor flowfield. It is possible that such interactions might produce

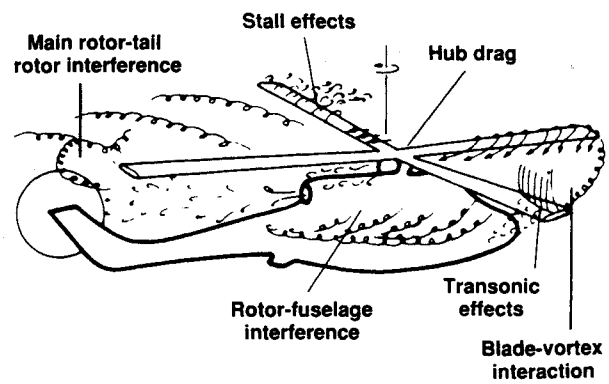

Fig. 1 Schematic of the complex flowfield of a helicopter in forward flight.

Presented as Paper 89-1848 at the AIAA 20th Fluid Dynamics, Plasma Dynamics, and Lasers Conference, Buffalo, NY, June 12-14, 1989; received July 10, 1989; revision received Dec. 31, 1992; accepted for publication Feb. 2, 1993.

*Senior Staff Scientist, JAI Associates, Inc., P.O. Box 293, Mountain View, CA. Associate Fellow AIAA.

†Senior Research Scientist, U. S. Army Aeroflightdynamics Directorate—ATCOM. Fellow AIAA.

vortex-induced boundary-layer separation which results in a sudden loss of lift and increase in drag. An accurate simulation of the rotor flowfield, therefore, must consider the induced effects of the vortex wake including the blade-vortex interactions (BVI).

Numerical simulations of vortex wakes are being attempted only recently as bigger and faster computers have become available.[1] This and other investigations have had some limited success to date. On the other hand, carefully measured experimental data on the three-dimensional BVI have been made available recently.[2,3] But much of the progress in modeling these blade-vortex interactions has been hampered by the lack of development of theoretical and/or numerical techniques to preserve the structure of the concentrated vortices in the flowfield without significant diffusion. The study of blade-vortex interaction has been the subject of numerous recent research papers.[4–15] These studies have considered different methods of preserving the structure of the concentrated vortex while convecting in the flowfield. Among these, the vortex-fitting (also called the prescribed-vortex or perturbation method or split-potential formulation) technique has been demonstrated to be a very effective method in preserving the vortex even when the computational grid is sparse. The major drawback of this method is that it does not allow for the distortion of the vortex core. For interactions where the vortex does not impinge head-on onto the blade, this method has proven to have worked very effectively and economically[7,8] compared to a more exact formulation[5] that allows for vortex distortion.

The purpose of this study is to devise a numerical method for the solution of the Euler equations to calculate accurately the unsteady blade-vortex interactional flowfield. In particular, this paper will focus on demonstrating the ability to calculate an interaction flowfield, which is three dimensional and unsteady, for parallel and oblique blade-vortex interactions on a model helicopter rotor tested in a wind tunnel[2,3] at subsonic and transonic flow conditions.

Governing Equations and Numerical Scheme

The governing partial differential equations are the unsteady Euler equations. For generality, the equations are transformed from the inertial Cartesian reference frame (x, y, z, t) to the arbitrary curvilinear coordinate frame (ξ, η, ζ, τ) that moves with the blade, while retaining strong conservation law form to capture shock waves. The transformed equations can be written as[16]

$$\partial_\tau(\hat{Q}-\hat{Q}_o)+\partial_\xi(\hat{F}-\hat{F}_o)+\partial_\eta(\hat{G}-\hat{G}_o)+\partial_\zeta(\hat{H}-\hat{H}_o)=0 \quad (1)$$

where

$$\hat{Q}=\frac{1}{J}\begin{bmatrix}\rho\\ \rho u\\ \rho v\\ \rho w\\ e\end{bmatrix}, \qquad \hat{F}=\frac{1}{J}\begin{bmatrix}\rho U\\ \rho uU+\xi_x p\\ \rho vU+\xi_y p\\ \rho wU+\xi_z p\\ UH-\xi_t p\end{bmatrix}$$

$$\hat{G}=\frac{1}{J}\begin{bmatrix}\rho V\\ \rho uV+\eta_x p\\ \rho vV+\eta_y p\\ \rho wV+\eta_z p\\ VH+\eta_t p\end{bmatrix}, \qquad \hat{H}=\frac{1}{J}\begin{bmatrix}\rho W\\ \rho uW+\zeta_x p\\ \rho vW+\zeta_y p\\ \rho wW+\zeta_z p\\ WH-\zeta_t p\end{bmatrix} \quad (2)$$

Here $\hat{Q}$ is the vector of the conserved flow variables, namely, the density ρ, the three mass fluxes ρu, ρv, and ρw in the three coordinate directions, and the total energy per unit volume e. Similarly, $\hat{Q}_o$ is a vector of the conserved flow variables corresponding to the solution of the Euler equations for a prescribed line vortex aligned with the uniform freestream of Mach number M_∞ in the y direction and convecting with the flow as shown in Fig. 2. The vectors $\hat{F}$, $\hat{G}$, $\hat{H}$, and $\hat{F}_o$, $\hat{G}_o$, $\hat{H}_o$ represent the appropriate flux terms for the two flows, respectively. These flux vectors, as shown, are scaled by the Jacobian J, e.g., $\hat{Q}=J^{-1}Q$, etc. The contravariant velocity components U, V, and W are defined as

$$U=\xi_t+\xi_x u+\xi_y v+\xi_z w$$

$$V=\eta_t+\eta_x u+\eta_y v+\eta_z w$$

$$W=\zeta_t+\zeta_x u+\zeta_y v+\zeta_z w$$

In the present formulation, ξ lies in the chordwise or wraparound direction, η is in the spanwise direction, and ζ is normal to the blade surface. The terms ξ_t, ξ_x, ξ_y, ξ_z, etc., are the coordinate transformation metrics.[16]

The velocity components u, v, w, and the pressure p are related to the total energy per unit volume e through the equation of state for a perfect gas by

$$p=(\gamma-1)\,[e-(\rho/2)(u^2+v^2+w^2)] \quad (3)$$

This equation of state, together with Eq. (1), completes the necessary equations that give the entire flowfield description. These equations are nondimensional. The reference length and velocity scales used are the chord of the blade C and the freestream speed of sound a_∞, respectively. All length scales are normalized by C and time by C/a_∞. The primitive variables of Eq. (1), namely, the density ρ, the mass fluxes ρu, ρv, ρw, and the energy per unit volume e, are normalized by the freestream reference quantities made up of ρ_∞ and a_∞ and the pressure p by γp_∞.

In the present formulation, Eq. (1) is solved in the inertial reference frame with the boundary conditions applied on the rotating blade. The terms u, v, and w are the Cartesian com-

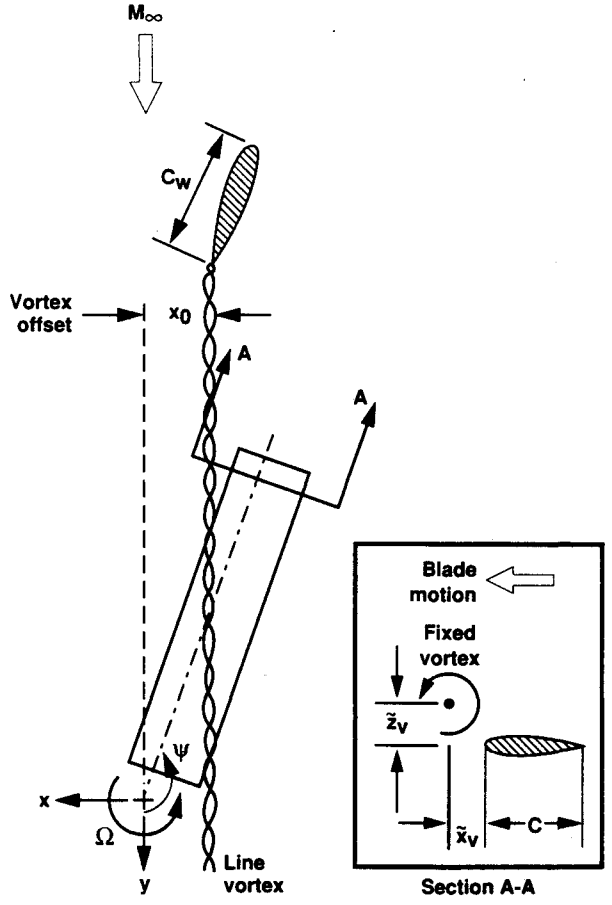

Fig. 2 Schematic of an advancing rotor blade passing a line vortex in a wind-tunnel experiment (Ref. 3).

ponents of velocity in the inertial coordinate system (x, y, z, t). The inertial coordinates $X = (x, y, z, t)$ are related to the blade-fixed coordinates $X_b = (\tilde{x}, \tilde{y}, \tilde{z})$ through the relation given by[17]

$$X(x, y, z) = \mathcal{R}(t)X_b(\tilde{x}, \tilde{y}, \tilde{z}), \qquad t = \tilde{t} \tag{4}$$

where $\mathcal{R}(t)$ is the rotational matrix.[18] For a rigid rotor that neglects the rotor disk attitude, blade flapping, and pitching motions, the rotational matrix can be written as

$$\mathcal{R}(t) = \frac{1}{J}\begin{bmatrix} \cos \Omega\tilde{t} & -\sin \Omega\tilde{t} & 0 \\ \sin \Omega\tilde{t} & \cos \Omega\tilde{t} & 0 \\ 0 & 0 & 1 \end{bmatrix} \tag{5}$$

Here Ω is the angular velocity of the rotor and Ωt represents the azimuthal sweep of the rotor blade.

The governing equations are solved using a two-factor, implicit, finite difference numerical scheme. The numerical algorithm that was originally developed by Ying et al.[19] has been modified to accommodate a prescribed-vortex perturbation formulation for a rotating blade environment. The numerical scheme uses spatial central differencing in the η and ζ directions and upwind differencing in the ξ direction. The two-factored scheme containing the vortex-fitting terms is given by

$$\begin{aligned} &[I + h\delta_\xi^b(\hat{A}^+)^n + h\delta_\zeta\hat{C}^n - D_i|_\zeta] \\ &\times [I + h\delta_\xi^f(\hat{A}^-)^n + h\delta_\eta\hat{B}^n - D_i|_\eta](\Delta\hat{Q}^n - \Delta\hat{Q}_o^n) \\ &= -\Delta t\{\delta_\xi^b[(\hat{F}^+)^n - (\hat{F}_o^+)^n] + \delta_\xi^f[(\hat{F}^-)^n - (\hat{F}_o^-)^n] \\ &+ \delta_\eta(\hat{G}^n - \hat{G}_o^n) + \delta_\zeta(\hat{H}^n - \hat{H}_o^n)\} \\ &- (D_e|_\eta + D_e|_\zeta)(\hat{Q}^n - \hat{Q}_o^n) \end{aligned} \tag{6}$$

where $h = \Delta t$ for first-order time accuracy; δ is typically a three-point, second-order-accurate, central difference operator; and the operators δ_ξ^b and δ_ξ^f are backward and forward three-point difference operators. The time index is denoted by n such that $t = (n\Delta t)$, and $\Delta\hat{Q}^n = \hat{Q}^{n+1} - \hat{Q}^n$. The flux vector $\hat{F}$ has been split into $\hat{F}^+$ and $\hat{F}^-$, according to its eigenvalues,[20] and the Jacobian matrices $\hat{A}^\pm$, $\hat{B}$, and $\hat{C}$ result from the local linearization of fluxes about the previous time level.[16] In writing Eq. (6), it is assumed that $\hat{A}_o^\pm \approx \hat{A}^\pm$, $\hat{B}_o \approx \hat{B}$, and $\hat{C}_o \approx \hat{C}$ where the Jacobian matrices $\hat{A}_o^\pm$, $\hat{B}_o$, and $\hat{C}_o$ correspond to the prescribed-vortex flowfield. In the absence of vortex interaction, the prescribed-disturbance flowfield reduces to a freestream. The finite difference scheme described in Eq. (6) uses flux splitting in ξ direction and central differencing in the η and ζ directions. As a consequence, numerical dissipation terms D_i and D_e are used in the η and ζ directions, and are given as combinations of second and fourth differences. For example, these terms in η direction are given by

$$\begin{aligned} D_e|_\eta &= (\Delta t)J^{-1}(|\eta|_x + |\eta|_t + |\eta|_z) \\ &\times \left[\epsilon_2\bar{\delta}\frac{|\bar{\delta}^2 p|}{|(1+\bar{\delta}^2)p|}\bar{\delta} + \epsilon_4\bar{\delta}^4\right]\Bigg|_\eta J \end{aligned} \tag{7a}$$

$$\begin{aligned} D_i|_\eta &= (\Delta t)J^{-1}(|\eta|_x + |\eta|_y + |\eta|_z) \\ &\times \left[\epsilon_2\bar{\delta}\frac{|\bar{\delta}^2 p|}{|(1+\bar{\delta}^2)p|}\bar{\delta} + 3\epsilon_4\bar{\delta}^4\right]\Bigg|_\eta J \end{aligned} \tag{7b}$$

where ϵ_2 and ϵ_4 are constants and $\bar{\delta}$ is a midpoint operator. In the vicinity of shock waves, the fourth-difference terms can cause oscillations, so it is desirable to drop these terms and rely only on the second-difference terms.

The factored operators are solved by sweeping in the ξ direction and inverting tridiagonal matrices with 5×5 blocks for the other two directions. Currently, a significant part of the computational time is taken to form the plus and minus Jacobian matrices for the flux vector $\hat{F}$ with this numerical scheme. However, this effort has been reduced by computing $\hat{A}^+$ and $\hat{A}^-$ at every other point (in both η and ζ directions) and averaging to obtain the matrices at the intermediate points. The numerical algorithm is second-order accurate in space and first order in time and the code is vectorized for the Cray-2 supercomputer.

A body-conforming finite difference grid has been used for the rectangular blade having an aspect ratio of 7 and consists of a warped spherical O–O grid topology. The flowfield grid is generated using the three-dimensional hyperbolic grid solver of Steger and Chaussee[21] with proper clustering in the leading- and trailing-edge regions and in the tip region. The grid is nearly orthogonal at the surface, the spacing in the normal direction at the surface is chosen to be $0.02C$, and all of the calculations were done on a $21 \times 101 \times 15$ points grid. The grid boundary is located at 8 chords in all directions.

The boundary conditions, both surface and far field, are applied explicitly. The slip conditions use an extrapolation of contravariant velocities to the surface. The density at the wall is determined by the zeroth-order extrapolation. The pressure along the body surface is calculated from the normal momentum relation (see, e.g., Ref. 16). Having calculated the density and pressure, the total energy is determined from the equation of state.

At the far-field boundary, the flow quantities are either fixed or extrapolated from the interior depending on whether the flow is subsonic or supersonic and if it is of inflow- or outflow-type at the boundary.[22,23] The characteristic velocities of the Euler equations determine the number of flow properties to be specified to control the reflections of waves from the boundaries. For the subsonic-inflow boundary, four quantities are specified and one quantity is determined. The four specified here are a Riemann invariant, the entropy, and two tangential velocities; the quantity that is calculated is also a Riemann invariant. For the supersonic inflow, all flow quantities are specified. At the subsonic-outflow boundaries, only one quantity is specified. For the supersonic-outflow condition all flow quantities are extrapolated from the interior. The plane containing the blade root is chosen very close to the rotation axis of the blade (at $R = 1.0C$) and is also treated as a far-field boundary.

The concentrated line vortex generated upstream of the rotor by a rectangular wing is fixed in the inertial space along a line of constant x. It is assumed to have an analytical representation for the cylindrical velocity distribution given by

$$v_\theta = \frac{C_k\hat{\Gamma}}{2\pi r}\left(\frac{r^2}{r^2 + a_o^2}\right) \tag{8}$$

The constant C_k in the preceding expression has been determined to be equal to 0.8 by matching the peak tangential velocity with the experimentally measured value at the measured radial distance.[8] The constant a_o is approximately equal to the radius of the viscous core of the vortex, and this is equal to the experimentally measured value of $0.167C$. The induced velocity field due to this line vortex is calculated using the Biot-Savart law and the pressure field is calculated by solving the radial momentum equation.

Results and Discussion

All of the calculations performed in this study are done in a time-accurate manner. Three test cases have been chosen for calculations from among the many test conditions of the two sets of experiments of Caradonna et al.[2,3] for parallel and oblique blade-vortex interactions. Since one of the purposes of the experiments was to collect data to validate numerical methods, the experimental apparatus was kept simple to ease the representation by numerical methods. The rotor geometry consists of a two-bladed rigid rotor of approximately 14-chord

diameter. The blades have a rectangular planform and are made up of NACA 0012 airfoils with no twist or taper. The rotor blades are set at zero collective pitch and are, therefore, essentially nonlifting in the absence of the vortex interaction. The interacting vortex was generated upstream of this rotor by a lifting NACA 0015 rectangular wing. Parallel blade-vortex interaction flowfields were generated by positioning the line vortex along the y axis ($x_o = 0.0$). Similarly, the oblique BVI flowfields were generated by moving the position of the line vortex such that it is still aligned along the y axis with $x_o < 0.0$. This enables the advancing rotor blade to encounter the line vortex continuously in the first and second quadrants of the azimuthal travel as shown in Fig. 2.

Although the main focus of the present investigation is to calculate the parallel and oblique blade-vortex interactions, it is necessary to first calculate the baseline flowfields of rotor-alone configuration (in the absence of vortex interaction) at the same freestream conditions. Two sets of results for parallel blade-vortex interactions, corresponding to $M_{tip} = 0.6$ and 0.8 and $\mu = 0.2$, and one set of results for oblique blade-vortex interaction corresponding to $M_{tip} = 0.763$ and $\mu = 0.197$, will be presented in the following sections and compared with the experimental data.

Rotor-Alone Case

The calculation of the rotor-alone flowfield solutions serves two purposes. First, it enables an understanding of the importance of unsteady time-lag effects in shock-wave growth and decay as well as the three dimensionality of the flowfield of the advancing rotor under transonic flow conditions. Second, it provides the baseline solution for starting the unsteady calculations of the vortex-interaction flowfield.

Figure 3 shows the instantaneous surface pressure distributions for various azimuthal positions of advancing rotor for the flow condition of $M_{tip} = 0.6$ and $\mu = 0.2$. Examination of these results suggests that at this reference station of $r_B = 0.893$ and for the subcritical flow condition, the flow behaves as if it is quasisteady and quasi-two dimensional. In spite of the gradual increase of the blade-element relative speed in the first quadrant and gradual decrease of the same in the second quadrant, the flowfield appears to remain nearly the same at all azimuthal locations, indicating that the unsteady time-lag effects are virtually absent for this flow condition and that the flow behaves as if it is quasisteady. In fact, also shown in Fig. 3 is the quasisteady surface pressures for one azimuth location of $\Psi = 90$ deg, which is in perfect agreement with the unsteady surface pressures at different azimuthal positions. Also, the comparison of these three-dimensional results with the two-dimensional results of Ref. 8 further confirms that the two

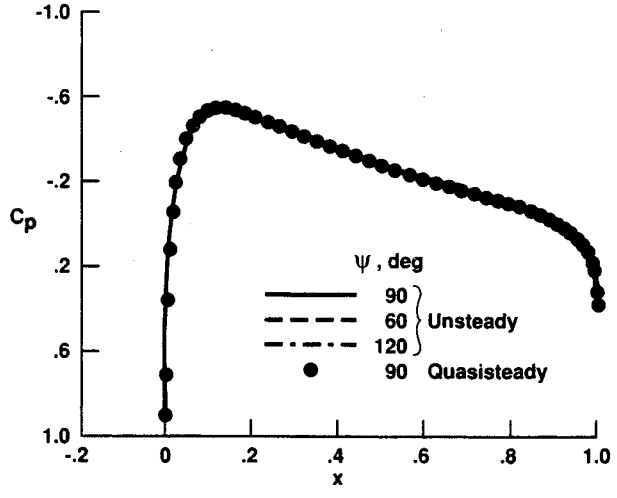

Fig. 3 Comparison of calculated surface pressures for an advancing rotor with the quasisteady surface pressures ($M_{tip} = 0.6$, $\mu = 0.2$, and $r_B = 0.893$).

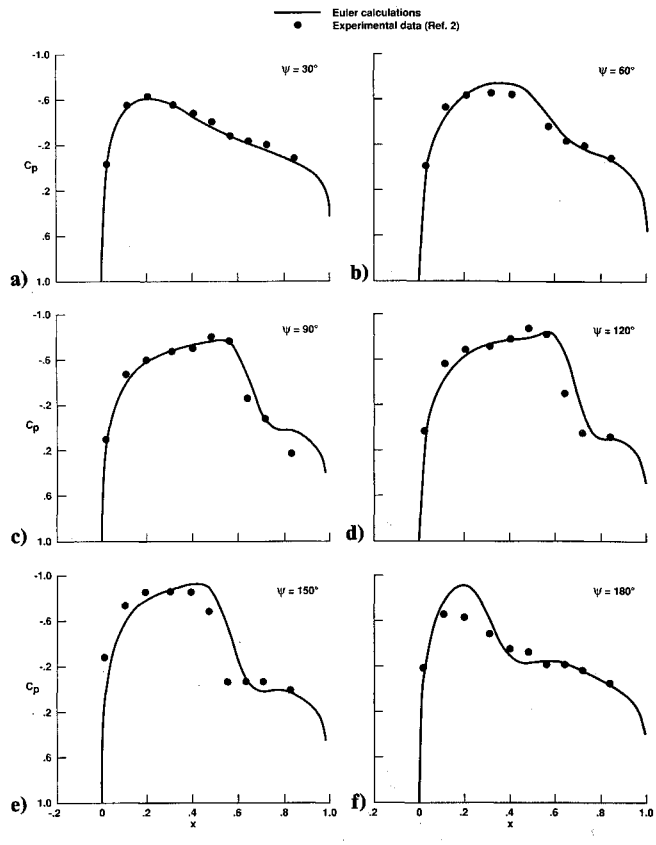

Fig. 4 Instantaneous surface pressure distributions at the reference blade section for advancing rotor ($M_{tip} = 0.8$, $\mu = 0.2$, and $r_B = 0.893$).

results are nearly identical, suggesting that the flow also behaves as if it is quasi-two dimensional.

At the supercritical tip flow conditions, corresponding to $M_{tip} = 0.8$ and $\mu = 0.2$, the basic rotor flowfield is dominated by the presence of a strong shock wave on the advancing blade over large parts of the first and second quadrants. The instantaneous surface pressures for the advancing rotor are shown in Fig. 4 at the radial station $r_B = 0.893$ for different azimuthal positions of the rotor blade. The results show good agreement with the experiments for all azimuthal locations. The absence of viscosity and therefore the boundary layer causes the Euler results to overpredict the shock strength and position in the first and second quadrants of azimuthal travel. The experimental data shows that the strong shock wave which was present at the beginning of the second quadrant nearly decays by the time the blade reaches $\Psi = 180$-deg position. In contrast, the numerical method predicts that the shock wave continues to persist at least until after it passes the $\Psi = 180$-deg azimuthal location. In fact, it is completely absent by the time the rotor blade reaches $\Psi = 184$-deg position. Previous two-dimensional Navier-Stokes calculations of the same flow[8] had shown strong three dimensionality and unsteady time lags in shock-wave growth and decay. The two-dimensional assumption for this flow essentially overpredicted the shock-wave position and strength, unlike the subcritical flow condition. In contrast, the three-dimensional Euler results seem to follow the experimental observation correctly.

Thus at this transonic flow condition, the flowfield is highly three dimensional, and exhibits strong unsteady time-lag behavior in the shock-wave formation and eventual demise. The unsteady time-lag characteristic of the flowfield is demonstrated in the surface pressure distributions of Fig. 4 shown for $\Psi = 60$-deg and 120-deg azimuthal positions, which shows that the two results are very different from each other.

In principle, the shock wave should attain its maximum strength when the relative flow speed reaches a maximum

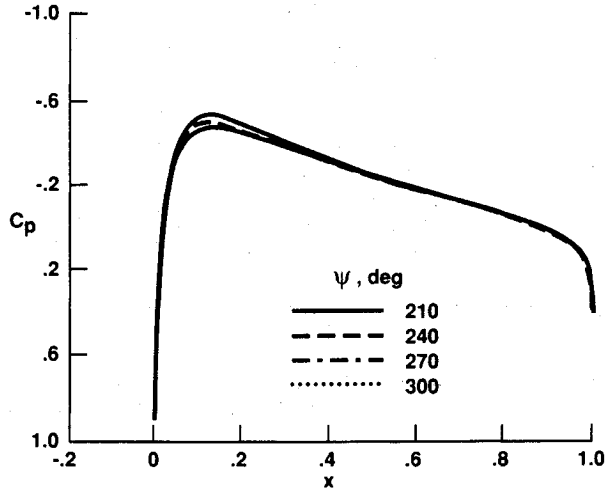

Fig. 5 Instantaneous surface pressure distributions at the reference blade section for retreating blade ($M_{tip} = 0.8$, $\mu = 0.2$, and $r_B = 0.893$).

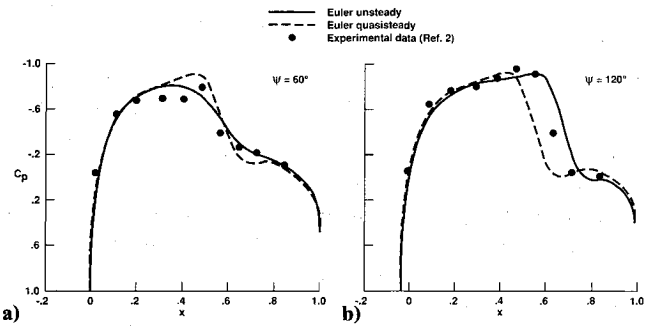

Fig. 6 Comparison of quasisteady and unsteady surface pressures for advancing rotor ($M_{tip} = 0.8$, $\mu = 0.2$, and $r_B = 0.893$).

value for $\Psi = 90$-deg blade azimuthal position. However, the shock wave keeps growing in strength even after the blade has passed the $\Psi = 90$-deg azimuthal position and a weak shock wave seems to persist even at the $\Psi = 180$-deg azimuth. The strengthening of the shock wave in the first quadrant and beyond, and the slow demise of it in the second quadrant, suggests the existence of a strong unsteady time-lag effect at this flow condition. Such a behavior was totally absent at the subcritical flow condition. The presence of the shock wave seems to introduce not only the time lag in the adjustment of the flow as the blade sweeps in azimuth, but also makes the flow highly three dimensional.

However, this behavior is confined to the advancing side of the rotor blade. In contrast, the flowfield of the retreating side appears really benign for this nonlifting rotor. The lingering effects of the shock wave, persisting at $\Psi = 180$ deg, soon die out as the blade sweeps into the third quadrant. Shown in Fig. 5 are the surface pressure distributions for several azimuthal locations of the blade in the third and fourth quadrants on the retreating cycle. Since the flowfield is basically subcritical on the retreating side, the instantaneous surface pressures of Fig. 5 appear to have the same behavior as those of Fig. 3.

The decay of the strong time-lag effects on the retreating blade allows a simplification in starting the unsteady calculations, but only if the strongest transonic region is avoided initially. To illustrate this point, Fig. 6 shows the quasisteady and unsteady surface pressures for the case of $M_{tip} = 0.8$ and $\mu = 0.2$ at the azimuthal locations of $\Psi = 60$ deg and 120 deg. For this flow condition, the results indicate that the quasisteady assumption overpredicts the shock strength at $\Psi = 60$ deg and underpredicts at $\Psi = 120$ deg. However, at $\Psi = 0.0$-deg position, the quasisteady and unsteady results are nearly identical, even for this flow condition. Therefore, it is still reasonable to start the unsteady calculations from the quasisteady solution calculated at $\Psi = 0.0$-deg azimuthal location.

Parallel Blade-Vortex Interaction

During the unsteady three-dimensional close encounter of a curved tip vortex with a rotating blade, the helicopter rotor undergoes a variety of blade-vortex interactions depending on the interaction angle between the leading edge of the rotating blade and the curved line vortex. These interactions are generally unsteady and three dimensional. One limiting case of such an encounter, for zero interaction angle, is termed parallel interaction (see, e.g., Ref. 7). In the experimental configuration considered here, this interaction occurs around $\Psi = 180$-deg azimuthal position. For an observer riding with the blade (at a given reference station along the span), it appears as though the observer is passing a fixed vortex in the flow. For this reason, this interaction is sometimes approximated as two-dimensional and unsteady.

To calculate accurately the blade-vortex interaction flowfield, it is necessary to preserve the vortex structure without numerical diffusion. As mentioned before, one method that has been demonstrated to work effectively and economically in achieving this is the prescribed-disturbance scheme.[7,8] The effectiveness of this scheme is illustrated in Fig. 7, showing the variation of lift coefficient as a function of vortex position during a two-dimensional airfoil-vortex interaction calculated using the Navier-Stokes, Euler, and transonic small-disturbance methods. Also shown in this figure is the Euler lift distribution calculated using a conventional (vortex capturing) technique.[24] Although the two Euler solutions are computed on the same grid, the numerical dissipation associated with the finite difference grids progressively weakens the gradients and reduces the effective vortex strength in the conventional method. Also, this numerical error is grid dependent (the finer the grid the lesser the error); however, it is completely absent in the prescribed-vortex solutions, which are essentially grid independent. Hence, the prescribed-disturbance method has been used here for preserving the vortex structure.

Subcritical Interaction

The results of a subcritical parallel BVI are discussed here. This case corresponds to the flow conditions of $M_{tip} = 0.6$, $\mu = 0.2$, and $C_k\hat{\Gamma} = 0.133$ at a blade reference station $r_B = 0.893$. The interacting vortex is located at $x_o = 0.0$ and $z_o = 0.4$ along the y axis. To calculate the BVI flowfield, the interacting vortex is introduced into the baseline rotor solution at the azimuthal position of $\Psi = 120$ deg. The unsteady flowfield is monitored as the blade is set in motion to advance in azimuth. The blade-vortex interaction effects peak around $\Psi = 180$-deg azimuthal position. The instantaneous surface pressure distributions are shown in Fig. 8 for several az-

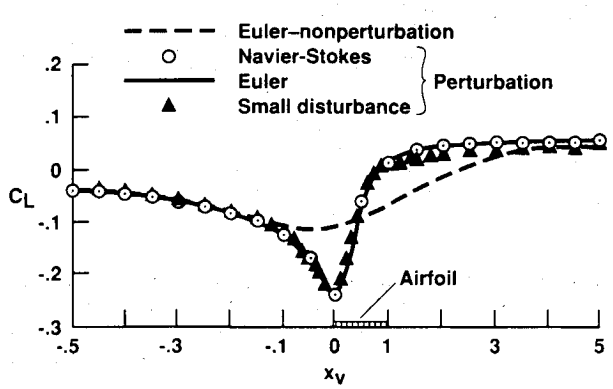

Fig. 7 Demonstration of prescribed-vortex method for preserving vortex structure in two-dimensional airfoil-vortex interaction: NACA 64A006 airfoil; $M_\infty = 0.85$, $\Gamma = 0.2$, and $z_v = -0.26$.

imuthal locations. The present results are compared with the experimental data[2] and the results from published two-dimensional Navier-Stokes calculations.[8]

The present results are in very good agreement with both the experimental data and the two-dimensional Navier-Stokes results. As seen from Fig. 8a for $\Psi = 178.15$ deg, the lift on the blade, which is initially zero in the absence of vortex interaction, is negative. Because of the sense of its rotation, the approaching vortex introduces a downwash in the flow immediately ahead of the blade. The lift rapidly becomes positive as the blade passes the line vortex. This crossover of lift, from negative to positive, seems to occur when the vortex is approximately aligned with the quarter-chord line of the blade (corresponding to $\tilde{x}_v = 0.0$). As mentioned before, the two-dimensional approximation of this three-dimensional, unsteady interaction is, in fact, a very good assumption for this subcritical flow condition. The close agreement of the viscous and inviscid results suggests that the viscous effects are unimportant for this relatively weak interaction.

Supercritical Interaction

This case corresponds to the flow condition of $M_{tip} = 0.8$, $\mu = 0.2$, and $C_k\hat{\Gamma} = 0.177$ at a blade reference station of $r_B = 0.893$. The interacting vortex location is the same as in the subcritical case. As in the rotor-alone case this flow condition, in contrast to the subcritical flow condition, exhibits strong unsteady time-lag effects in shock-wave growth and decay for the advancing rotor. This feature seems to accentuate the three-dimensional nature of the flow, and a two-dimensional approximation of this flow overpredicts the shock-wave strength and location, as demonstrated in Ref. 8.

As before, to calculate the BVI flowfield, the interacting vortex is introduced at $\Psi = 120$-deg azimuthal position, and the time evolution of the flow is monitored as the blade advances in azimuth. Figure 9 shows the interaction flowfield results in terms of instantaneous surface pressures for several azimuthal positions of the blade. Also shown in these figures are the experimental data.[2] The present results are in good agreement with the experimental data for all azimuthal locations of the blade, and they capture the essential details of the flow sharply, including the shock waves.

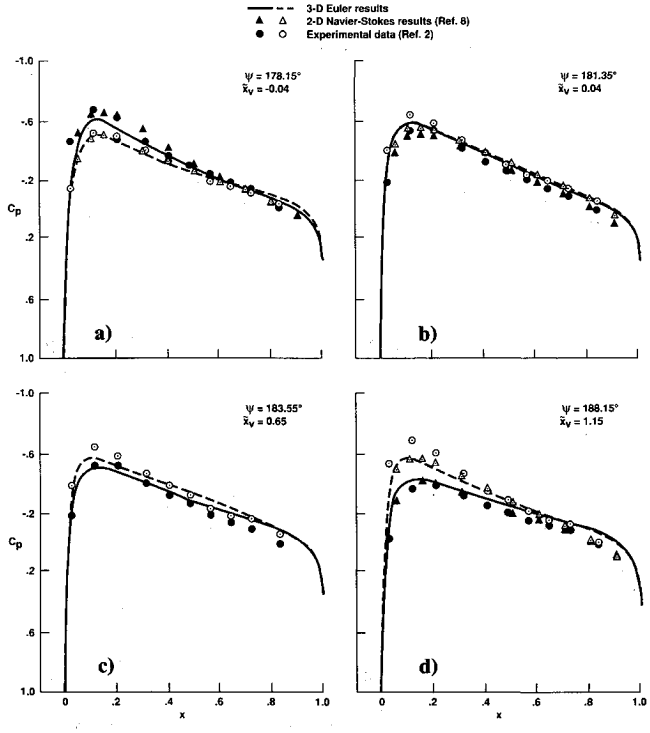

Fig. 8 Comparison of instantaneous surface pressures during parallel blade-vortex interaction for subsonic case ($M_{tip} = 0.6$, $\mu = 0.2$, $C_k\hat{\Gamma} = 0.133$, $x_o = 0.0$, $z_o = 0.4$, and $r_B = 0.893$).

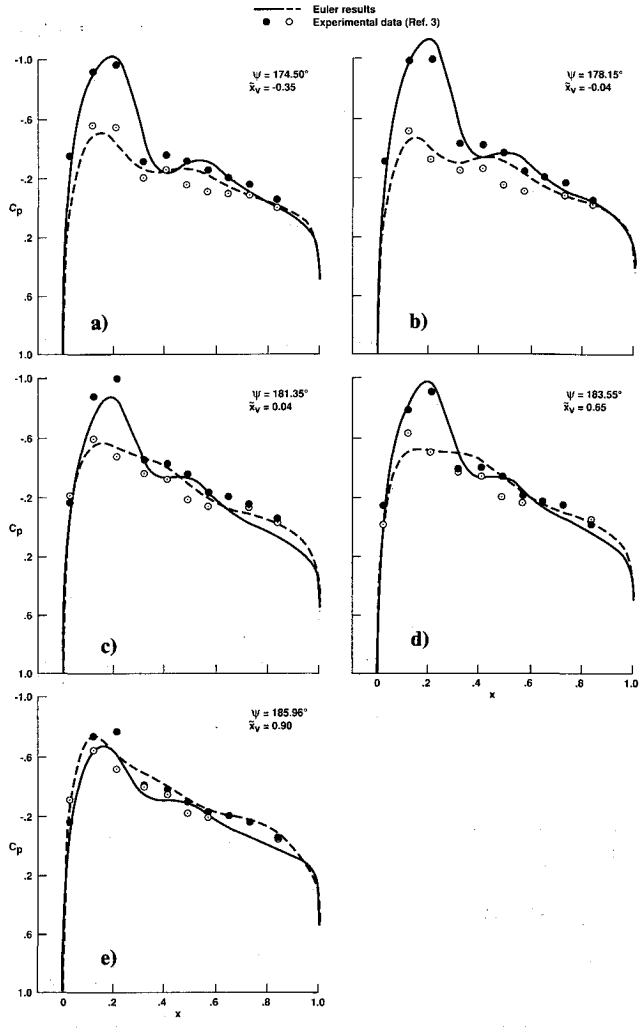

Fig. 9 Comparison of instantaneous surface pressures during parallel blade-vortex interaction for transonic case ($M_{tip} = 0.8$, $\mu = 0.2$, $C_k\hat{\Gamma} = 0.177$, $x_o = 0.0$, $z_o = 0.4$, and $r_B = 0.893$).

The effect of vortex interaction is to induce time-dependent aerodynamic forces on the rotor. For example, as seen from the surface pressure plots of Fig. 9, the lift on the blade, which is initially zero, becomes negative due to induced downwash and rapidly increases to a positive value as the blade passes the stationary vortex. The peak effects of the interaction appear to occur when the blade leading edge is approximately above the line vortex.

Oblique Blade-Vortex Interaction

An interaction is called oblique when the line vortex interacts over a large part of the blade in the radial direction at any given instant of its azimuthal travel. In other words, an observer fixed to the blade and moving with it sees at any given instant different parts of the line vortex interacting with the blade as it sweeps from 0 to 180 deg in azimuth (in the present case). As seen in the schematic of Fig. 2, an oblique interaction is therefore possible whenever x_o is nonzero. This is in contrast to the parallel blade-vortex interaction that occurs when $x_o = 0.0$ where an observer located at one radial station sees the blade passing a point vortex that is stationary. The observer is therefore concerned about the influence of the entire line vortex at this particular radial station. Therefore, for an observer stationed on the blade, the interaction experienced of parallel and oblique BVI is uniquely different.

The oblique interaction considered here corresponds to a freestream condition of $M_{tip} = 0.763$ and $\mu = 0.197$. The interacting vortex located at $x_o = -2.13$ and $z_o = 0.25$ has a

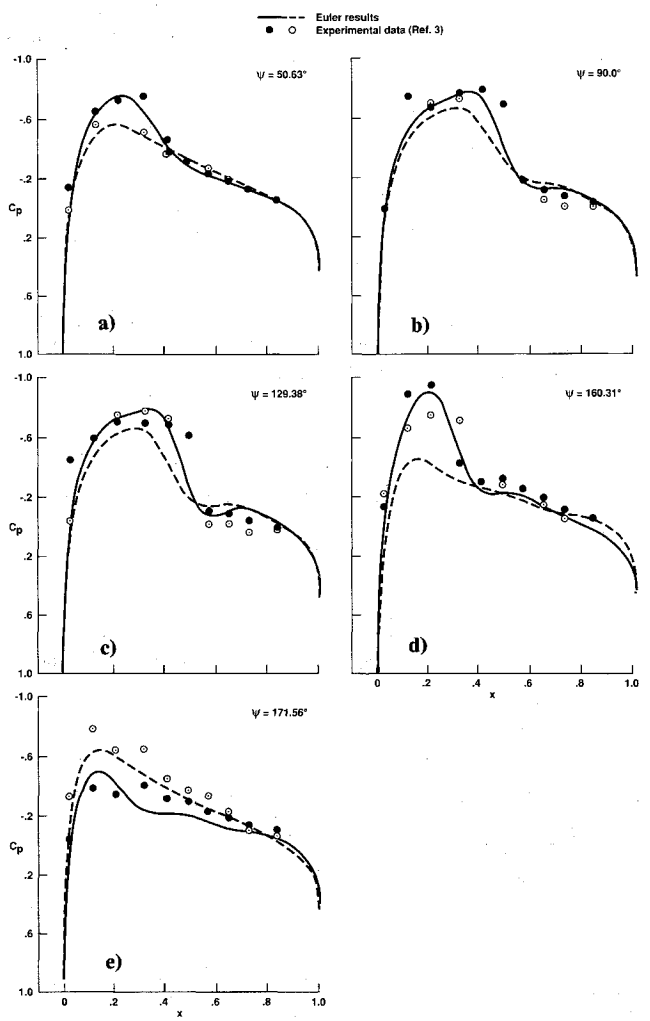

Fig. 10 Comparison of instantaneous surface pressures during oblique blade-vortex interaction for transonic case ($M_{tip} = 0.763$, $\mu = 0.197$, $C_k\hat{\Gamma} = 0.179$, $x_o = -2.13$, $z_o = 0.25$, and $r_B = 0.946$).

strength of $C_k\hat{\Gamma} = 0.179$ for the reference blade section at $r_B = 0.946$. In contrast to the parallel interaction, the oblique interaction occurs over a larger azimuthal sweep of the rotor blade, starting in the first quadrant and completing in the second quadrant. The peak interaction occurs at around $\Psi = 20$ deg in the first quadrant and around $\Psi = 160$ deg in the second quadrant. Therefore, the vortex is introduced into the flow at $\Psi = 0.0$ deg in this case, and the evolution of the unsteady interacting flow is monitored for the advancing rotor.

Figure 10 shows the calculated instantaneous surface pressure distributions at several azimuthal positions of the blade and the experimental data.[3] The comparison of results shows overall agreement of surface pressures. This set of experimental data appears to have large scatter. Even the surface pressures of rotor-alone case have similar scatter.[25] The interaction in the first quadrant occurs at subcritical flow and the agreement with data is good at $\Psi = 50$ deg. The interaction in the second quadrant occurs under supercritical flow condition. The maximum relative blade tip speed in this case (for $\Psi = 90$-deg position) is 0.91 compared to a value of 0.96 corresponding to the transonic parallel interaction case and is thus a weaker interaction.

From the surface pressures of Fig. 10 it can be seen that the lift on rotor blade, which is initially zero, becomes negative due to the vortex influence (because of the sense of rotation), increases to a maximum (negative) value in the second quadrant, and changes over to a positive value at about $\Psi = 165$-deg azimuthal position of the blade. The peak interaction appears to occur around the $\Psi = 160$-deg azimuthal position.

Conclusions

A numerical procedure is presented to calculate the unsteady, inviscid, three-dimensional flowfields of a helicopter rotor in forward flight encountering parallel and oblique blade-vortex interactions in subsonic and transonic flow conditions. Important flow features such as unsteady time-lag effects in shock-wave growth and demise, as well as the importance of three-dimensional effects, are discussed. Although it is possible under certain flow conditions to approximate the parallel blade-vortex interaction as two dimensional and unsteady, the oblique blade-vortex interaction, on the other hand, is strongly three dimensional and unsteady, and therefore cannot be approximated as two-dimensional interaction.

The numerical results are compared with two sets of experimental data generated by Caradonna et al.[2,3] on a model two-bladed rotor in a wind tunnel. The present Euler results show good agreement with experiments for both the parallel and oblique interactions at subsonic and transonic flow conditions. Thus, the numerical methodology presented here has demonstrated the ability to accurately calculate the flowfield of an advancing helicopter rotor including the effects of vortex interaction.

Acknowledgments

The first author (GRS) would like to acknowledge the support of this research by the U. S. Army Research Office under Contract DAAL03-88-C-0006 and DAAL03-90-C-0013. Computational time was provided by the Applied Computational Fluids Branch of NASA Ames Research Center. The authors would like to dedicate this paper to the memory of J. L. Steger.

References

[1]Srinivasan, G. R., McCroskey, W. J., Baeder, J. D., and Edwards, T. A., "Numerical Simulation of Tip Vortices of Wings in Subsonic and Transonic Flows," *AIAA Journal,* Vol. 26, No. 10, 1988, pp. 1153–1162.

[2]Caradonna, F. X., Laub, G. H., and Tung, C., "An Experimental Investigation of the Parallel Blade-Vortex Interaction," 10th European Rotorcraft Forum, The Hague, The Netherlands, Aug. 1984; also NASA TM-86005, Nov. 1984.

[3]Caradonna, F. X., Lautenschlager, J., and Silva, M., "An Experimental Study of Rotor Blade-Vortex Interactions," AIAA Paper 88-0045, Jan. 1988.

[4]Workshop on Blade-Vortex Interactions (unpublished), NASA Ames Research Center, Moffett Field, CA, Oct. 1984.

[5]Rai, M. M., "Navier-Stokes Simulation of Blade-Vortex Interaction Using High-Order Accurate Upwind Schemes," AIAA Paper 87-0543, Jan. 1987.

[6]Steinhoff, J., and Suryanarayanan, K., "The Treatment of Vortex Sheets in Compressible Potential Flow," AIAA Paper 83-1881-CP, July 1983.

[7]Srinivasan, G. R., and McCroskey, W. J., "Numerical Simulations of Unsteady Airfoil-Vortex Interactions," *Vertica,* Vol. 11, No. 1/2, 1987, pp. 3–28.

[8]Srinivasan, G. R., McCroskey, W. J., and Baeder, J. D., "Aerodynamics of Two-Dimensional Blade-Vortex Interaction," *AIAA Journal,* Vol. 24, No. 10, 1986, pp. 1569–1576.

[9]Wu, J. C., Sankar, N. L., and Hsu, T. M., "Unsteady Aerodynamics of an Airfoil Encountering a Passing Vortex," AIAA Paper 85-0203, Jan. 1985.

[10]Strawn, R. C., and Tung, C., "The Prediction of Transonic Loading on Advancing Helicopter Rotors," NASA TM-88238, April 1986.

[11]Caradonna, F. X., Strawn, R. C., and Bridgeman, J. O., "An Experimental and Computational Study of Rotor-Vortex Interactions," *Vertica,* Vol. 12, No. 4, 1988, pp. 315–327.

[12]George, A. R., and Lyrintzis, A. S., "Acoustics of Transonic Blade-Vortex Interactions," *AIAA Journal,* Vol. 26, No. 7, 1988, pp. 769–776.

[13]Lyrintzis, A. S., and George, A. R., "Far-Field Noise of Transonic Blade-Vortex Interactions," *American Helicopter Society Journal,* Vol. 34, No. 3, pp. 30–39.

[14]Baeder, J. D., McCroskey, W. J., and Srinivasan, G. R., "Acoustic Propagation Using Computational Fluid Dynamics," *Proceedings of the 42nd Annual Forum of the American Helicopter Society,* The American Helicopter Society, Washington, DC, June 1986, Vol. 1,

pp. 551–562.

[15]Damodaran, M., and Caughey, D. A., "A Finite Volume Euler Calculation of the Aerodynamics of Transonic Airfoil-Vortex Interaction," *AIAA Journal,* Vol. 26, No. 11, 1988, pp. 1346–1353.

[16]Pulliam, T. H., and Steger, J. L., "Implicit Finite-Difference Simulations of Three-Dimensional Compressible Flow," *AIAA Journal,* Vol. 18, No. 2, 1980, pp. 159–167.

[17]Srinivasan, G. R., and McCroskey, W. J., "Navier-Stokes Calculations of Hovering Rotor Flowfields," *Journal of Aircraft,* Vol. 25, No. 10, 1988, pp. 865–874.

[18]Isom, M. P., "Unsteady Subsonic and Transonic Potential Flow Over Helicopter Rotor Blades," NASA CR-2463, Oct. 1974.

[19]Ying, S. X., Steger, J. L., Schiff, L. B., and Baganoff, D., "Numerical Simulation of Unsteady, Viscous, High-Angle-of-Attack Flows Using a Partially Flux-Split Algorithm," AIAA Paper 86-2179, Aug. 1986.

[20]Steger, J. L., and Warming, R. F., "Flux Vector Splitting of the Inviscid Gasdynamic Equations with Application to Finite-Difference Methods," *Journal of Computational Physics,* Vol. 40, No. 2, 1981, pp. 263–293.

[21]Steger, J. L., and Chaussee, D. S., "Generation of Body-Fitted Coordinates Using Hyperbolic Partial Differential Equations," *SIAM J. Sci. Stat. Comput.,* Vol. 1, No. 4, 1980, pp. 431–437.

[22]Jameson, A., Schmidt, W., and Turkel, E., "Numerical Solution of the Euler Equations by Finite Volume Methods Using Runge-Kutta Time-Stepping Schemes," AIAA Paper 81-1259, June 1981.

[23]Chakravarthy, S. R., "Euler Equations—Implicit Schemes and Boundary Conditions," *AIAA Journal,* Vol. 21, No. 5, 1983, pp. 699–706.

[24]Srinivasan, G. R., Chyu, W. J., and Steger, J. L., "Computation of Simple Three-Dimensional Wing-Vortex Interaction in Transonic Flow," AIAA Paper 81-1206, June 1981.

[25]Srinivasan, G. R., and McCroskey, W. J., "Unsteady Interaction of a Rotor With a Vortex," AIAA Paper 89-1848, June 1989.